Nano Lett. Author manuscript; available in PMC 2019 May 31.

Published in final edited form as:
Nano Lett. 2016 July 12; 16(7): 4282–4287. doi:10.1021/acs.nanolett.6b01335.

Shape and inter-helical spacing of DNA origami nanostructures studied by small angle X-ray scattering

Stefan Fischer[#], **Caroline Hartl**[#], **Kilian Frank**, **Joachim O. Rädler**, **Tim Liedl**[#*], and **Bert Nickel**[#*]

Fakultät für Physik and Center for NanoScience, Ludwig-Maximilians-Universität, Geschwister-Scholl-Platz 1, 80539 München, Germany

[#] These authors contributed equally to this work.

Abstract

Scaffolded DNA origami nanostructures enable the self-assembly of arbitrarily shaped objects with unprecedented accuracy. Yet varying physiological conditions are prone to induce slight structural changes in the nanoscale architecture. Here, we report on high precision measurements of overall shape and inter-helical distance of three prototypic DNA origami structures in solution using synchrotron small angle X-ray scattering. Sheet-, brick- and cylinder-shaped DNA constructs were assembled and the shape factors determined with Ångström resolution from fits to the scattering profiles. With decreasing $MgCl_2$ concentration electrostatic swelling of both, shape cross section and inter-helical DNA spacing, of the DNA origami structures is observed. The structures tolerate up to 10% inter-helical expansion before they disintegrate. In contrast, with increasing temperature, the cylinder-shaped structures show no thermal expansion in a wide temperature window before they abruptly melt above 50°C. Details on molecular structure of DNA origami can also be obtained using in-house X-ray scattering equipment and hence allow for routine folding and stability testing of DNA based agents that are designed to operate under varying salt conditions.

Keywords

SAXS; DNA Nanotechnology; DNA self-assembly; magnesium; folding; melting

DNA self-assembly is a powerful resource in the attempt to take control of matter on the nanoscale1–4. A wide variety of custom-shaped DNA nanostructures have been presented over the last decades, many of them serving as platforms to precisely arrange other components such as fluorophores, nanoparticles or proteins5–11. One of the most commonly used methods in the field of DNA nanotechnology nowadays is DNA origami. Here, a phage-derived, long "scaffold" strand is folded with a set of short "staple" oligonucleotides into the desired shape12. The assembled DNA origami objects usually are comprised of multiple parallel helices that are arranged in sheets or in a hexagonal or square lattice cross section13, 14. Holliday junctions formed by scaffold or staple strands interconnect the

---

[*] Corresponding author: tim.liedl@lmu.de (Phone: +498921803725), nickel@lmu.de (Phone: +498921801460).

Conflict of Interest: The authors declare no competing financial interest.

helices. High-resolution atomic force microscopy (AFM) maps of the canonical 2D origami sheet already revealed that the interconnects between parallel helices induce a chicken wire-like network of the helices that are zigzagging along their axis 12. The analysis of the inner fine structure of 3D DNA origami objects so far has been based on Cryo transmission electron microscopy (TEM) studies 14, 15 revealing an average inter-helical gap on the order of 0.6 nm for the square lattice arrangement, which is similar to the gap between helices in the 2D sheets 12. Thus, the structural design of DNA origami constructs is well established allowing the assembly of defined scaffolds for nanoscale placement of ligands.

While computational tools predict the overall shape of the DNA objects rather well16–18, the influence of varying physiological conditions is not yet well understood. In particular the presence of ions such as Na^+, Mg^{2+}, Ca^{2+}, which are involved in the regulation of many cellular processes, was found to strongly influence the efficiency of DNA origami folding13, 19. Clearly, in order to understand the molecular mechanism that prompts ionic sensitivity, it is instructive to monitor the structural changes of DNA origami *in situ* as even moderate structural changes will have impact on the use of DNA origami as platforms for precise molecular positioning9, 20 or as drug delivery vehicles21, 22. However, distortion-free *in situ* studies of solvent induced changes of the 3D internal structure are challenging. High-speed AFM can highlight dynamic aspects23 and fluorescence resonance energy transfer (FRET) allows to study selected intra-molecular distances9, 10, 20. Regular EM imaging is performed in vacuum and CryoEM at low temperatures. Collecting full 3D information furthermore involves collecting data from many samples and from all possible orientations, which makes the construction of 3D EM images a cumbersome task15, 24.

In contrast, small angle X-ray scattering (SAXS) allows for analysis of molecular assemblies in solution at ambient conditions. For example, inter-helical distances have been determined in dispersed lipid-DNA and polymer-DNA complexes25, 26 as well as in helical fiber bundles27. So far, SAXS was employed only sporadically to study DNA origami, *e.g.* to confirm the successful assembly of gold particle-DNA lattices28 and to characterize some shape aspects of rather open 3D objects such as a DNA nanocage29 and octahedral shapes30. However, none of these studies included high resolution data nor performed form factor analysis.

Here, we determined the folded shape in solution and the inter-helical packing distance for three prototypic DNA origami constructs from synchrotron SAXS experiments with sub-Ångström precision. We thus were able to observe and quantify the electrostatic expansion of the inner DNA origami spacing and ultimately the loss of stability with decreasing $MgCl_2$ concentrations. Furthermore, we use SAXS to monitor folding and unfolding of DNA origami as a function of temperature. Remarkably, our studied DNA origami structures do not expand thermally before melting. Finally, we demonstrate that also in-house X-ray equipment allows for determination of origami structure in solution and hence for validation of DNA designs under physiological conditions.

Shape and inner structure of DNA Origami: sheet, brick, and cylinder

Three DNA origami structures were assembled, concentrated, and analyzed via SAXS. As a first structure, we selected a twist-corrected variant of the canonical one-layer sheet of parallel DNA helices (Figure 1a)12. Second, we investigated a brick-like object built of three layers of parallel helices arranged on a square lattice (three-layer block)9, 14. In this design all inner helices are connected to four neighboring helices (Figure 1b). Third, we used a cylinder-like structure6 of the honeycomb-lattice type13, where each of the inner helices is connected to three neighboring helices (24-helix bundle, Figure 1c).

Imaging with TEM or liquid tapping mode AFM confirmed successful and high-yield assembly of all three objects. The concentration of each structure was estimated by absorption spectroscopy. For SAXS measurements we worked with concentrations of ˜ 250 nM, which corresponds to 1.25 mg/ml of DNA (molecular weight of all structures ˜ 5 MDa). Concentrated DNA origami samples were initially probed with our in-house SAXS setup31 and experimental data with superior statistics in the low intensity region were obtained at synchrotron sources (P08 at DESY and ID1 at ESRF). The SAXS data for our three model systems (sheet, brick, cylinder) together with design schemes and TEM and AFM micrographs are summarized in Figure 1. The SAXS intensity distributions for the three model structures show very distinct and characteristic curves in log-log representation of scattered intensity (I) versus the scattering vector (q). In our experiments the q-values cover the range from 0.01 Å^{-1} to 0.3 Å^{-1}. This interval corresponds to real space distances of 2 nm up to about 60 nm, *i.e.* the X-ray data contains information on the overall origami shapes and their inner structure.

On first sight, the intensity of the monolayer sheet exhibits a q^{-2} behavior for small q values as predicted from Porod’s law for two-dimensional objects32. The scattering signal of the brick shows different slopes in the log-log plot owing to its three different lateral dimensions and a dip at 0.08 Å^{-1} due to its thickness. The cylindrical 24-helix bundle has the most pronounced scattering features due to its rotational symmetry. The minima and maxima of the scattered intensity stem from the radius of the helix bundle. For the detailed form factor, we refer to the Supplementary Information (Eq. 3).

We analyzed our data by geometric models, which approximate the origami structures by homogeneous geometric bodies. We here use the analytical Fourier transform of a sheet, brick or cylinder, respectively and we account for free oligonucleotides in solution by adding a Debye background with a radius of gyration R_g representing a Gaussian chain29, 33. As the objects are oriented randomly in solution, we integrated numerically over all possible angles between the axis of the objects and their q-vector. For small q values up to 0.15 Å^{-1}, this model matches the intensity for all three objects (gray lines in Fig 1).

Overall the dimensions obtained from the geometric model analysis agree very well with the design parameters. The sheet has a thickness A = 21.5 ± 0.3 Å, a width B = 610 ± 60 Å, while the length C was fixed to 960 Å. The brick has a length C = 627± 5 Å, a width B = 379 ± 2 Å and thickness A = 76.6 ± 0.2 Å. The 24-helix bundle modeled as a cylinder has a radius of 78.7 ± 0.2 Å. Note that the uncertainties diverge when the characteristic dimensions approach the resolution limit. Dimensions that are too large to be resolved by the SAXS experiments, such as the cylinder length of L = 100 nm, do not influence our analysis. Exact fit parameter values for all dimensions can be found in the Supplementary Table S2.

In all cases, the geometric model is not able to describe the scattered intensities in the region of high q values (0.15-0.3 Å^{-1}). This q region corresponds to real space distances of 2.1 nm - 4.2 nm, *i.e.* here the inner structure of the DNA origami is probed. In order to refine our model in this region, we represented each DNA double helix by a straight cylinder with diameters of 2.0 nm and 2.2 nm. The distance between the cylinders is varied until this model reproduced the observed peak positions in the high q region (blue curves in Figure 1 shows solution for 2.2 nm diameter). These peaks represent the Bragg condition of the inner arrangements of the DNA double helices that arise from the different lattice design principles (linear, square and hexagonal; unit cells are shown in Figure 1).

This model, however, consistently overestimates the inter-helical peak intensities. Since we idealize the electron distribution of a DNA double helix by a full cylinder, we neglect atomistic structure. Using more realistic but still analytical helix models including a continuous single helix34 and a continuous double helix improved the quality of the fits only slightly. Simulations of scattering intensities calculated from (quasi-)atomistic models obtained from computational tools17, 18, 35, 36, on the other hand, resulted in good intensity matching for the 24-helix bundle. Unfortunately, this procedure did not improve the fits for the other two structures suggesting that these models require refinement. A problem here may be the well-known chicken wire-like structure of the DNA helices in DNA origami12, 14, 15, which is not taken care of in the above models. Therefore, we combine the geometric model with a Lorentzian peak centered at $q_0=2\pi/d$, probing the helical lattice planes d (cf. Supporting Information Eq. 7-10). This model yields nearly perfect description of all the experimental intensity data (red line in Figure 1). In detail, for the one layer sheet, we obtain an inter-helical distance of 26.9 ± 0.2 Å, similar to the cubic lattice spacing of the brick, which is 27.32 ± 0.02 Å. The inter-helical distance measured for the honeycomb lattice of the 24-helix bundle is 25.36 ± 0.03 Å. These values agree well with lattice parameters obtained from CryoEM, where an effective helix diameter of 2.6 nm was observed15 and from molecular dynamic simulations37, 38. Note that all these literature values have been obtained under buffer conditions that favour DNA origami stability, *i.e.* 10 mM or more of Mg^{2+} and temperatures below 30 °C. We will now address the question to which extend origami structure and shape change with temperature and ionic strength.

Structural changes of a DNA origami structure upon exposure to different MgCl$_2$ concentrations

We expose the 24-helix bundle to different Mg^{2+} concentrations at room temperature. The scattering of the samples in buffer of 0, 1, 2, 3, 5 and 11 mM MgCl$_2$ is summarized in Figure 2A. The typical oscillations of the scattering intensity are recognizable for all samples down to 2 mM MgCl$_2$. However, with decreasing Mg^{2+} concentration, characteristic features are less pronounced and the scattering at low q drops significantly. Ultimately, for a MgCl$_2$ content of 1 mM and 0 mM, the origami scattering features vanish completely. The remaining scattering intensity is a combination of the general Debye background (cf. Eq. S5) and a second Debye term with a Radius of gyration of about 20 nm, which can be considered as a contribution from the dismantled DNA origami structure. Complementary TEM micrographs support this scenario qualitatively, *i.e.* we still find predominantly intact structures for 2 mM $MgCl_2$ and only dismantled objects at 1 mM and 0 mM $MgCl_2$ (Figure 2B).

In order to quantify the structural changes in response to the $MgCl_2$ concentration, we evaluated both, the inter-helical distance and the diameter of the whole origami cylinder (Figure 2C). With decreasing $MgCl_2$ content both values increase up to 10% in a strongly correlated manner before the structures fully dismantle (cf. Supplementary Figure S5).

The expansion as a function of decreasing salt reflects the interplay of the electrostatic repulsion between the negatively charged DNA phosphate backbone and the elastic restoring forces of the internal DNA origami crossovers within the origami framework. The electrostatic Coulomb potential is well known to be screened by salt27, 37 and increases at reduced ionic strengths. Interestingly, the relative change of the inter-helical distance mirrors the behavior of the calculated Debye length of the Mg^{2+} ions (Figure 2C) suggesting that the main role of the Mg^{2+} ions is Debye screening rather than specific effects such as ion bridging39. This observation is in line with molecular dynamics simulations, which have already shown that the origami frameworks prevents the proper relative orientation of the DNA double helix needed to form ion bridges in the first place37, 40. Note that the observed origami lattice expansion prior to disassembly of up to 10% is rather characteristic for classical solids, while hydrogels show orders of magnitude larger swelling capability. Reducing the number of crossovers might allow to tune the origami mesh swelling, *e.g.* for the fabrication of molecular sieves.

Annealing and melting of DNA Origami Structures

Next we study the annealing and melting of a 24-helix bundle origami by ramping the temperature while recording x-ray data. We focus on two parameters, which highlight different structural aspects of folded DNA origami architectures; first, the scattered intensity in the limit of small q, which is a measure for the fraction of folded structures (Figure 3A) and second, the intensity of the inter-helical peak (Figure 3B). Upon heating, both parameters initially show little temperature dependence suggesting most structures stay intact. Rising the temperature to 50°C and beyond, results in a drastic drop of the concentration of folded structures. At the same time the inter-helical peak vanishes completely, which suggests abrupt melting. In order to quantify this melting process, we plot the normalized intensities versus temperature (Figure 3C). Both parameters exhibit the typical shape of a melting transition at 53.5°C.

Interestingly, we do not observe significant thermal expansion prior to melting, *i.e.* the inter-helical peak at $q \sim 0.17$ $Å^{-1}$ and the dip at $q \sim 0.05$ $Å^{-1}$, which are sensitive to the inter-helical distance and origami cylinder radius, respectively, remain at a fixed q-position until the whole structure melts and the intensities vanish. This indicates that thermal fluctuations, e.g. Helfrich undulation forces do not play a major role in the force balance. In contrast, the electrostatically induced disassembly exhibited a continuous lattice expansion at low ionic strengths, indicating that the microscopic mechanism for thermal melting is fundamentally different from electrostatically driven disassembly. These results suggest that the 24-helix bundle should be able to act as rigid framework in the whole physiologically relevant temperature range of up to 50°C. Both distinct structural transitions provide a critical test for thermodynamic models of DNA origami constructs that take ionic and temperature effects into account.

Along these lines it is remarkable that the melting behavior of the three-layered brick shows subtle differences when compared to that of the 24-helix bundle. The dip in the sheet scattering curve, which is sensitive to the sheet thickness, vanishes well below the overall melting transition (cf. Supplementary Figure S2). This premelting phenomenon could result either from the difference between square (3-layered brick) and hexagonal (24-helix bundle) lattice arrangements or from the different geometries, *i.e.* brick *vs.* rod.

Optimization of the reverse process of melting, i.e. folding of DNA into origami structures, is essential for high yield assembly of high quality DNA structures. It has been shown that for certain designs a specific folding temperature can be determined in fluorescence-based DNA melting assays41, 42. Generally, folding is a slow process occurring at lower temperature than melting. We thus followed the folding kinetics by cooling the sample down from a molten state and simultaneously monitoring the evolution of the SAXS signal at selected temperatures until the origami folding is completed (also confirmed by TEM imaging and agarose gel analysis, see Supplementary Figure S1 and S3). Our experiments confirm a clear temperature hysteresis between melting and folding (at 45°C) for the 24-helix bundle as shown in Figure 3C (blue triangles). Note that this type of data acquisition was possible at our in-house source as the underlying processes occur on time scales of hours and information can readily be obtained from the rather high scattering intensities at low q.

With the field of DNA nanotechnology advancing towards biotechnological, biomedical and materials applications, accurate structure determination of DNA constructs in varying environments and physiological conditions is essential. Moreover, assembly and disassembly as function of temperature and ionic strength are at the heart of precise and high yield production of DNA origami. We found that SAXS is a versatile tool to access structural details at the Ångström level surpassing imaging and fluorescence read-out approaches. Importantly, SAXS is an in-situ method that provides reliable data without the necessity for labeling or immobilization. We observed swelling of the inter-helical distance of up to 10% in response to Mg^{2+} depletion, which could in principle be used to transduce ionic strength or pH changes into conformational transitions. Tunable porosity or pH dependent structures may have potential applications for retention and release of drug cargo by DNA-based agents. From a theoretical viewpoint the finite ionic and zero thermal expansion revealed by SAXS scattering are remarkable and leave room for refined 3D origami models that include thermal melting and electrostatic interactions in various ionic conditions. A better understanding of temperature and ionic effects on DNA origami will help to improve stability issues in complex fluids and potentially allow for purposeful structural switching mechanisms.

Supplementary Material

Refer to Web version on PubMed Central for supplementary material.

Acknowledgements

This work was supported by the ERC Starting Grant ORCA, by the DFG through the cluster of excellence *Nanosystems Initiative Munich* and the SFB1032 (Project A6, A7). We acknowledge support during beam time at DESY (P08, Uta Ruett) and ESRF (ID1, Jan Hilhorst). We thank Jan Lipfert for helpful discussions. This work benefitted from SasView software,originally developed by the DANSE project under NSF award DMR-0520547.

References

(1). Seeman NC. J Theor Biol. 1982; 99:237–247. [PubMed: 6188926]

(2). Seeman NC. Annu Rev Biochem. 2010; 79:65–87. [PubMed: 20222824]

(3). Jones MR, Seeman NC, Mirkin CA. Science. 2015; 347:840.

(4). Zheng JP, Birktoft JJ, Chen Y, Wang T, Sha RJ, Constantinou PE, Ginell SL, Mao CD, Seeman NC. Nature. 2009; 461:74–77. [PubMed: 19727196]

(5). Tan SJ, Campolongo MJ, Luo D, Cheng WL. Nat Nanotechnol. 2011; 6:268–276. [PubMed: 21499251]

(6). Kuzyk A, Schreiber R, Fan ZY, Pardatscher G, Roller EM, Hogele A, Simmel FC, Govorov AO, Liedl T. Nature. 2012; 483:311–314. [PubMed: 22422265]

(7). Ding BQ, Deng ZT, Yan H, Cabrini S, Zuckermann RN, Bokor J. J Am Chem Soc. 2010; 132:3248. [PubMed: 20163139]

(8). Voigt NV, Torring T, Rotaru A, Jacobsen MF, Ravnsbaek JB, Subramani R, Mamdouh W, Kjems J, Mokhir A, Besenbacher F, Gothelf KV. Nat Nanotechnol. 2010; 5:200–203. [PubMed: 20190747]

(9). Stein IH, Schuller V, Bohm P, Tinnefeld P, Liedl T. Chemphyschem. 2011; 12:689–695. [PubMed: 21308944]

(10). Stein IH, Steinhauer C, Tinnefeld P. J Am Chem Soc. 2011; 133:4193–4195. [PubMed: 21250689]

(11). Li HY, Park SH, Reif JH, LaBean TH, Yan H. J Am Chem Soc. 2004; 126:418–419. [PubMed: 14719910]

(12). Rothemund PWK. Nature. 2006; 440:297–302. [PubMed: 16541064]

(13). Douglas SM, Dietz H, Liedl T, Hogberg B, Graf F, Shih WM. Nature. 2009; 459:414–418. [PubMed: 19458720]

(14). Ke YG, Douglas SM, Liu MH, Sharma J, Cheng AC, Leung A, Liu Y, Shih WM, Yan H. J Am Chem Soc. 2009; 131:15903–15908. [PubMed: 19807088]

(15). Bai XC, Martin TG, Scheres SHW, Dietz H. P Natl Acad Sci USA. 2012; 109:20012–20017.

(16). Douglas SM, Marblestone AH, Teerapittayanon S, Vazquez A, Church GM, Shih WM. Nucleic Acids Res. 2009; 37:5001–5006. [PubMed: 19531737]

(17). Castro CE, Kilchherr F, Kim DN, Shiao EL, Wauer T, Wortmann P, Bathe M, Dietz H. Nat Methods. 2011; 8:221–229. [PubMed: 21358626]

(18). Kim DN, Kilchherr F, Dietz H, Bathe M. Nucleic Acids Res. 2012; 40:2862–2868. [PubMed: 22156372]

(19). Martin TG, Dietz H. Nat Commun. 2012; 3

(20). Funke JJ, Dietz H. Nat Nano. 2015

(21). Smith D, Schuller V, Engst C, Rädler JO, Liedl T. Nanomedicine-Uk. 2013; 8:105–121.

(22). Hahn J, Wickham SFJ, Shih WM, Perrault SD. Acs Nano. 2014; 8:8765–8775. [PubMed: 25136758]

(23). Endo M, Sugiyama H. Accounts Chem Res. 2014; 47:1645–1653.

(24). Kato T, Goodman RP, Erben CM, Turberfield AJ, Namba K. Nano Lett. 2009; 9:2747–2750. [PubMed: 19492821]

(25). Rädler JO, Koltover I, Salditt T, Safinya CR. Science. 1997; 275:810–814. [PubMed: 9012343]

(26). DeRouchey J, Netz RR, Rädler JO. Eur Phys J E. 2005; 16:17–28. [PubMed: 15688137]

(27). Chung PJ, Choi MC, Miller HP, Feinstein HE, Raviv U, Li Y, Wilson L, Feinstein SC, Safinya CR. Proceedings of the National Academy of Sciences. 2015; 112:E6416–E6425.

(28). Tian Y, Wang T, Liu WY, Xin HL, Li HL, Ke YG, Shih WM, Gang O. Nat Nanotechnol. 2015; 10:637. [PubMed: 26005999]

(29). Andersen ES, Dong M, Nielsen MM, Jahn K, Subramani R, Mamdouh W, Golas MM, Sander B, Stark H, Oliveira CLP, Pedersen JS, et al. Nature. 2009; 459:73–U75. [PubMed: 19424153]

(30). Oliveira CLP, Juul S, Jorgensen HL, Knudsen B, Tordrup D, Oteri F, Falconi M, Koch J, Desideri A, Pedersen JS, Andersen FF, et al. Acs Nano. 2010; 4:1367–1376. [PubMed: 20146442]

(31). Bruetzel LK, Fischer S, Salditt A, Sedlak SM, Nickel B, Lipfert J. Rev Sci Instrum. 2016; 87:025103. [PubMed: 26931887]

(32). Glatter, O, Kratky, O. Small angle X-ray scattering. Academic press; 1982.

(33). Roe, R-J. Methods of X-Ray and Neutron Scattering in Polymer Science. Oxford University Press; New York: 2000.

(34). Szekely P, Ginsburg A, Ben-Nun T, Raviv U. Langmuir. 2010; 26:13110–13129. [PubMed: 20695550]

(35). Yoo, J; Sobh, AN; Li, C-Y; Aksimentiev, A. cadnano to PDB File Converter. https://nanohub.org/resources/cadnanocvrt

(36). Svergun D, Barberato C, Koch MHJ. J Appl Crystallogr. 1995; 28:768–773.

(37). Arbona JM, Aime JP, Elezgaray J. Phys Rev E. 2012; 86

(38). Yoo J, Aksimentiev A. P Natl Acad Sci USA. 2013; 110:20099–20104.

(39). Qiu XY, Andresen K, Kwok LW, Lamb JS, Park HY, Pollack L. Phys Rev Lett. 2007; 99

(40). Luan B, Aksimentiev A. J Am Chem Soc. 2008; 130:15754. [PubMed: 18975864]

(41). Sobey TL, Renner S, Simmel FC. J Phys-Condens Mat. 2009; 21

(42). Sobczak JPJ, Martin TG, Gerling T, Dietz H. Science. 2012; 338:1458–1461. [PubMed: 23239734]

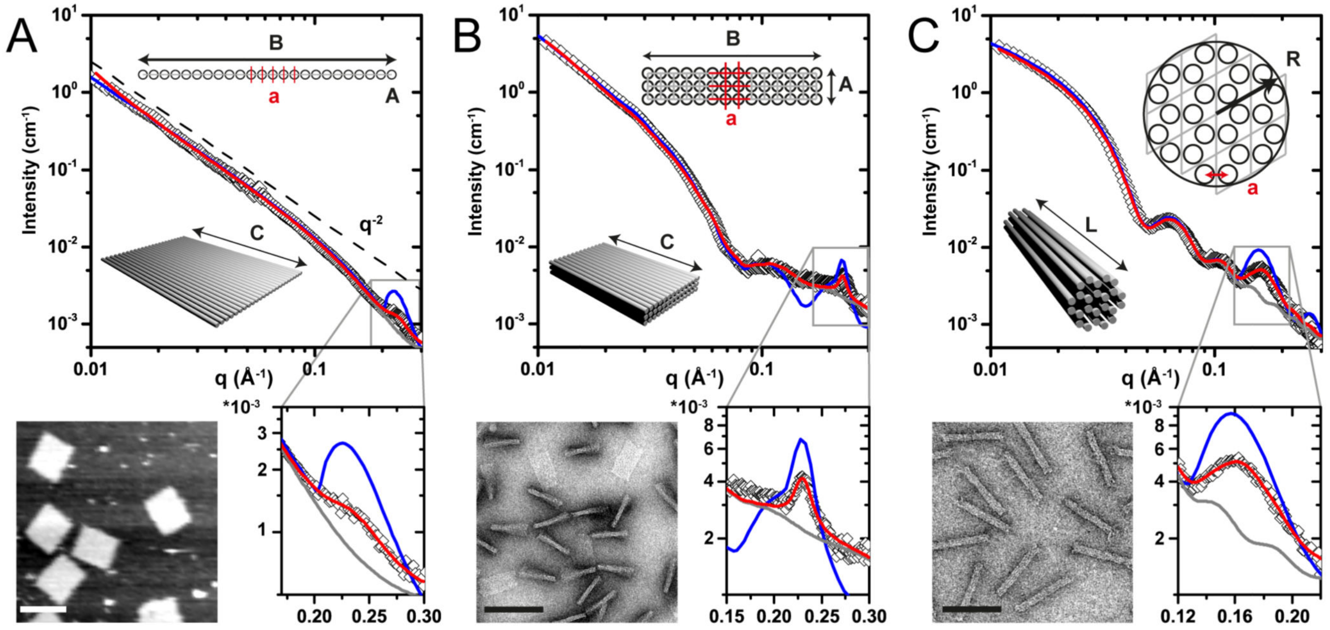

Figure 1.

Small angle X-ray scattering intensity of three different types of DNA origami structures in solution with corresponding model, lattice structure (with unit cell) and AFM or TEM image: (A) One-layer sheet, (B) Three-layer block with square lattice design and (C) 24-helix bundle with honeycomb lattice design. Three different model fits are shown for each intensity plot. The geometric model takes only the overall shape – *i.e.* sheet, block or cylinder – into account (gray lines). A model treating the double helices as rigid cylinders predicts the existence and position of a peak corresponding to inter-helical distance but overestimates the peak's intensity (blue lines). The combination of the geometric model with a Lorentzian peak attributed to the inter-helical arrangement reproduces the scattering intensity with high accuracy (red lines). Scale bars: 100 nm.

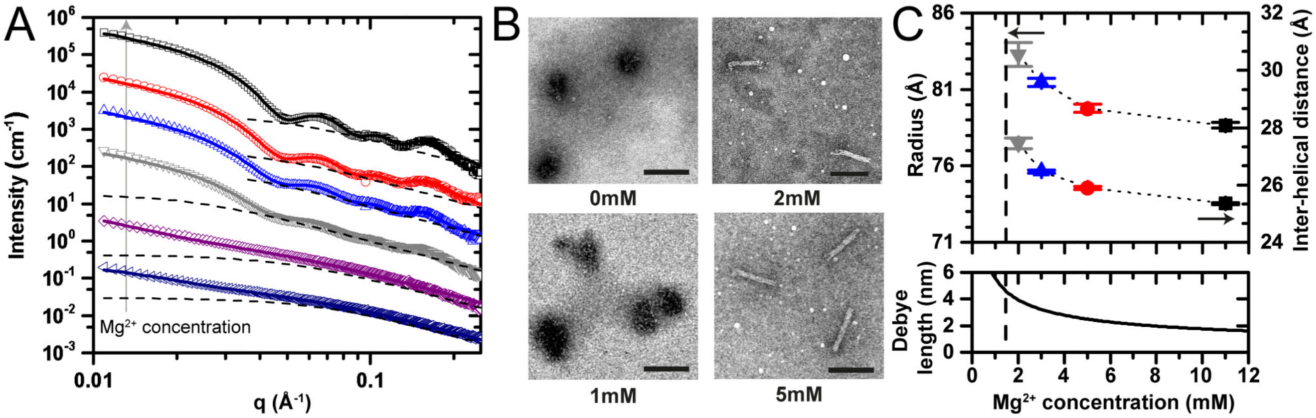

Figure 2.

(A) Scattering curves of 24-helix bundles at varying $MgCl_2$ concentrations (11 mM, 5 mM, 3 mM, 2 mM, 1 mM, 0 mM from top to bottom) with Debye background (dashed lines). (B) TEM images of DNA structures exposed to 0 mM, 1 mM, 2 mM and 5 mM $MgCl_2$. Scalebars: 100 nm. (C) Radii of the overall cylinder-shaped structure and inter-helical distances extracted from A and Debye length for the corresponding $MgCl_2$ concentrations.

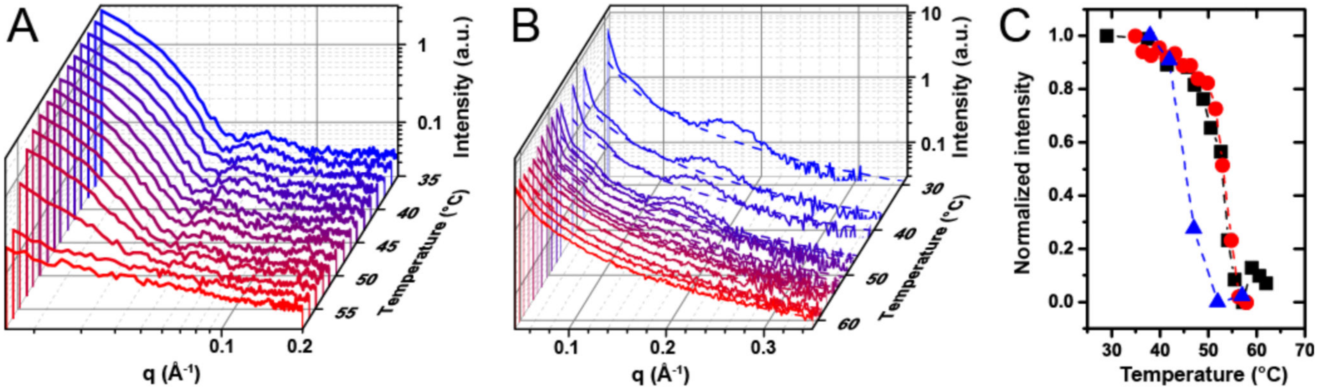

Figure 3.

In-situ SAXS measurements during melting of 24-helix bundles. (A) Scattering intensities for increasing temperatures (35 °C to 58 °C) recorded in-house. (B) Background-corrected intensities recorded between 29 °C and 62 °C at a synchrotron source (ID1@ESRF) to access higher q-values. (C) Normalized intensities at small q extracted from A (red circles) and helix peak intensities extracted from B (black squares) plotted as function of temperature. Melting occurs at higher temperatures than folding (extracted from Supplementary Figure S3, blue triangles).